

# BLADE: Filter Learning for General Purpose Computational Photography

Pascal Getreuer, Ignacio Garcia-Dorado, John Isidoro, Sungjoon Choi,  
Frank Ong, Peyman Milanfar

Google Research, Mountain View CA, USA

December 11, 2017

**Abstract** The Rapid and Accurate Image Super Resolution (RAISR) method of Romano, Isidoro, and Milanfar is a computationally efficient image upscaling method using a trained set of filters. We describe a generalization of RAISR, which we name Best Linear Adaptive Enhancement (BLADE). This approach is a trainable edge-adaptive filtering framework that is general, simple, computationally efficient, and useful for a wide range of problems in computational photography. We show applications to operations which may appear in a camera pipeline including denoising, demosaicing, and stylization.

## 1 Introduction

In recent years, many works in image processing have been based on nonlocal patch modeling. These include nonlocal means of Buades, Coll, and Morel [3] and the BM3D denoising method of Dabov et al. [7] and their extensions to other problems including deconvolution [14] and demosaicing [8, 9]. While these methods can achieve state-of-the-art quality, they tend to be prohibitively computationally expensive, limiting their practical use.

Deep learning has also become popular in image processing. These methods can trade quality vs. computation time and memory costs through considered choice of network architecture. Particularly, quite a few works take inspiration from partial differential equation (PDE) techniques and closely-connected areas of variational models, Markov random fields, and maximum a posteriori estimation. Roth and Black’s fields of experts [22], among other methods [24, 25, 34], develops forms of penalty functions (image priors) that are trainable. Schmidt and Roth’s cascade of shrinkage fields [25] and Chen and Pock’s trainable non-linear reaction diffusion [5] are designed as unrolled versions of variational optimization methods, with each gradient descent step or PDE diffusion step interpreted as a network

layer, then substituting portions of these steps with trainable variables. These hybrid deep learning/energy optimization approaches achieve impressive results with reduced computation cost and number of parameters compared to more generic structures like multilayer convolutional networks [5].

Deep networks are hard to analyze, however, which makes failures challenging to diagnose and fix. Despite efforts to understand their properties [1, 15, 18, 29], the representations deep networks learn and what makes them effective remain powerful but without a complete mathematical analysis. Additionally, the cost of running inference for deep networks is nontrivial or infeasible for some applications on mobile devices. Smartphones lack the computation power to do much processing in a timely fashion at full-resolution on the photographs they capture (often +10-megapixel resolution as of 2017). The difficulties are even worse for on-device video processing.

These problems motivate us to take a lightweight, yet effective approach that is *trainable* but still *computationally simple* and *interpretable*. We describe an approach that extends the Rapid and Accurate Image Super Resolution (RAISR) image upscaling method of Romano, Isidoro, and Milanfar [21] and others [6, 13] to a generic method for trainable image processing, interpreting it as a local version of optimal linear estimation. Our approach can be seen as a shallow two-layer network, where the first layer is predetermined and the second layer is trained. We show that this simple network structure allows for inference that is computationally efficient, easy to train, interpret, and sufficiently flexible to perform well on a wide range of tasks.

## 1.1 Related work

RAISR image upscaling [21] begins by computing the  $2 \times 2$  image structure tensor on the input low-resolution image. Then for each output pixel location, features derived from the structure tensor are used to select a linear filter from a set of a few thousand trained filters to compute the output upscaled pixel. A similar upscaling method is global regression based on local linear mappings super-interpolation (GLM-SI) by Choi and Kim [6], which like RAISR, upscales using trained linear filters, but using overlapping patches that are blended in a linearly optimal way. The  $L^3$  demosaicing method [13] is a similar idea but applied only to demosaicing.  $L^3$  computes several local features, including the patch mean, variance, and saturation, then for each pixel uses these features to select a linear filter<sup>1</sup> from among a trained set of filters to estimate the demosaiced pixel. In both RAISR and  $L^3$ , processing is locally adaptive due to the nonlinearity in filter selection. We show that this general approach extends well to other image processing tasks.

Quite a few other works use collections of trainable filters. For instance, Gelfand and Ravishanker [12] consider a tree where each node contains a filter, where in nonterminal nodes, the filter plus a threshold is used to decide which child branch to traverse. Fanello et al. [23] train a random forest with optimal linear filters at the leaves and split nodes to decide which

---

<sup>1</sup>More precisely,  $L^3$ 's trained filters are affine, they include a bias term.

filter to use. Schuler, Leistner, and Bischof [26] expands on this work by replacing the linear filters with polynomials of the neighboring pixels.

Besides  $L^3$ , probably the closest existing work to ours is the image restoration method of Stephanakis, Stamou, and Kollias [27]. The authors use local wavelet features to make a fuzzy partition of the image into five regions (one region describing smooth pixels, and four regions for kinds of details). A Wiener filter is trained for each region. During inference, each Wiener filter is applied and combined in a weighted sum according to the fuzzy partition.

The K-LLD method of Chatterjee and Milanfar [4] is closely related, where image patches with similar local geometric features are clustered and a least-squares optimal filter is learned for each cluster. The piecewise linear estimator of Yu, Sapiro, and Mallat [33] similarly uses an E-M algorithm that alternately clusters patches of the image and learns a filter for each cluster. Our work can be seen as a simplification of these methods using predetermined clusters.

## 1.2 Contribution of this work

We extend RAISR [21] to a trainable filter framework for general imaging tasks, which we call Best Linear Adaptive Enhancement (BLADE). We interpret this extension as a spatially-varying filter based on a locally linear estimator.

In contrast to Stephanakis [27], we make a hard decision at each pixel of which filter to apply, rather than a soft (fuzzy) one. Unlike Yu et al. [33], our filter selection step is a simple uniform quantization, avoiding the complication of a general nearest cluster search. Notably, these properties make our computation cost independent of the number of filters, which allows us to use many filters (often hundreds or thousands) while maintaining a fast practical system.

Specifically, unique attributes of our approach are:

- Inference is very fast, executing in real-time on a typical mobile device. Our CPU implementation for  $7 \times 7$  filters produces 22.41 MP/s on a 2017 Pixel phone.
- Training is solvable by basic linear algebra, where training of each filter amounts to a multivariate linear regression problem.
- The approach is sufficiently flexible to perform well on a range of imaging tasks.
- Behavior of the method is interpretable in terms of the set of trained linear filters, including diagnostics to catch problems in training.

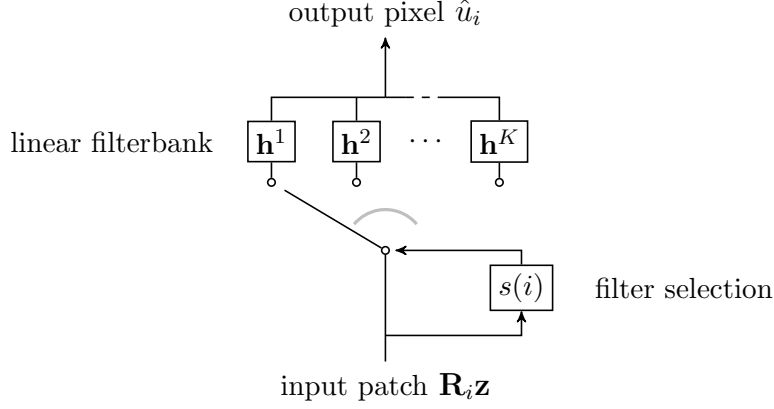


Figure 1: BLADE inference.  $\mathbf{R}_i$  denotes extraction of a patch centered at pixel  $i$ . For a given output pixel  $\hat{u}_i$ , we only need to evaluate the one linear filter that is selected,  $h^{s(i)}$ .

### 1.3 Outline

We introduce BLADE in section 2. Filter selection based on the image structure tensor is described in section 3. Sections 4 and sections 5, 6, and 7 demonstrate several applications of BLADE. Computational performance at inference is discussed in section 8. Section 9 concludes the paper.

## 2 Best Linear Adaptive Enhancement

This section introduces our Best Linear Adaptive Enhancement (BLADE) extension of RAISR.

We denote the input image by  $\mathbf{z}$  and subscripting  $z_i$  to denote the value at spatial position  $i \in \Omega \subset \mathbb{Z}^2$ . Let  $\mathbf{h}^1, \dots, \mathbf{h}^K$  be a set of linear FIR filters, where superscript indexes different filters and each filter has nonzero support or footprint  $F \subset \mathbb{Z}^2$ . Inference is a spatially-varying correlation. The essential idea of RAISR is that for inference of each output pixel  $\hat{u}_i$ , one filter in the bank is selected:

$$\hat{u}_i = \sum_{j \in F} h_j^{s(i)} z_{i+j}, \quad (1)$$

where  $s(i) \in \{1, \dots, K\}$  selects the filter applied at spatial position  $i$ . This spatially-adaptive filtering is equivalent to passing  $\mathbf{z}$  through a linear filterbank and then for each spatial position selecting one filter output (Figure 1). We stress that in computation, however, we only evaluate the one linear filter that is selected. Both the selection  $s$  and spatially-varying filtering (1) are vectorization and parallelization-friendly so that inference can be performed with high efficiency.

Let  $N = |F|$  be the filter footprint size. The number of arithmetic operations per output

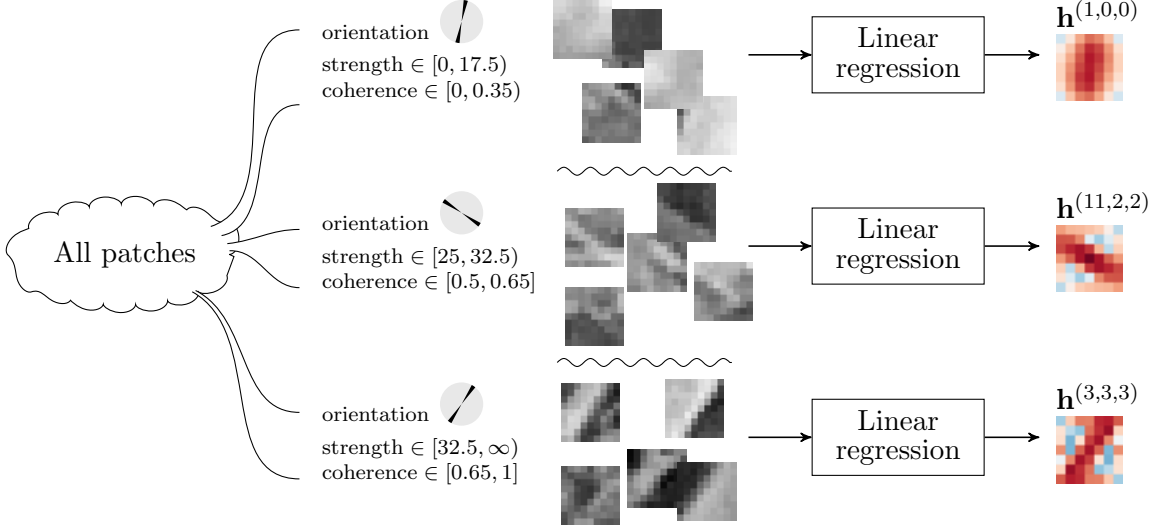


Figure 2: BLADE training. Linear filters are trained piecewise on different subsets of patches. Filter selection by local orientation, strength, and coherence (explained in section 3) partitions input patches into multiple subsets, and we regress a linear filter on each subset.

pixel in (1) is  $O(N)$ , proportional to the footprint size, independent of the number of filters  $K$  because we make a hard decision to select one filter at each pixel location. A large number of filters may be used without impacting computation time, so long as the filters fit in memory and filter selection  $s$  is efficient.

To make filtering adaptive to edges and local structure, we perform filter selection  $s$  using features of the  $2 \times 2$  image structure tensor (discussed in section 3). We determine the filter coefficients by training on a dataset of observed and target example pairs, using a simple  $L^2$  loss plus a quadratic regularizing penalty. This optimization decouples such that the filters are individually solvable in closed form, in which each filter amounts to a regularized multivariate linear regression [21].

## 2.1 Inference

Rewriting inference (1) generically,<sup>2</sup> each output pixel is an inner product between some selected filter and patch extracted from the input,

$$\hat{u}_i = (\mathbf{h}^{s(i)})^T \mathbf{R}_i \mathbf{z}, \quad (2)$$

where  $(\cdot)^T$  denotes matrix transpose and  $\mathbf{R}_i$  is an operator that extracts a patch centered at  $i$ ,  $(\mathbf{R}_i \mathbf{z})_j = z_{i+j}$ ,  $j \in F$ . The operation over the full image can be seen to be a matrix-vector multiplication,

$$\hat{\mathbf{u}} = \mathbf{W} \mathbf{z}, \quad (3)$$

<sup>2</sup>Yet more generically, signals could be vector-valued or on domains of other dimension, though we will focus on two-dimensional images.

where  $\mathbf{W}$  is a data-dependent matrix in which the  $i$ th row of  $\mathbf{W}$  is  $\mathbf{R}_i^T \mathbf{h}^{s(i)}$ .

## 2.2 Training

We use a quadratic penalty for filter regularization. Given an  $N \times N$  nonnegative definite matrix  $\mathbf{Q}$ , define the seminorm for a filter  $\mathbf{h}$

$$\|\mathbf{h}\|_{\mathbf{Q}} := (\mathbf{h}^T \mathbf{Q} \mathbf{h})^{1/2}. \quad (4)$$

For most applications, we set the regularizing  $\mathbf{Q}$  matrices such that  $\|\mathbf{h}\|_{\mathbf{Q}}$  is a discretization of  $L^2$  norm of the filter’s spatial gradient (also known as the  $H^1$  or Sobolev  $W^{1,2}$  seminorm),

$$\|\mathbf{h}\|_{\mathbf{Q}}^2 = \frac{\lambda}{2} \sum_{\substack{i,j \in F: \\ \|i-j\|=1}} |h_i - h_j|^2 \quad (5)$$

where  $\lambda$  is a positive parameter controlling the regularization strength. This encourages filters to be spatially smooth.

Given an observed input image  $\mathbf{z}$  and corresponding target image  $\mathbf{u}$ , we train the filter coefficients as the solution of

$$\arg \min_{\mathbf{h}^1, \dots, \mathbf{h}^K} \sum_{k=1}^K \|\mathbf{h}^k\|_{\mathbf{Q}}^2 + \|\mathbf{u} - \hat{\mathbf{u}}\|^2, \quad (6)$$

in which, as above,  $\hat{u}_i = (\mathbf{h}^{s(i)})^T \mathbf{R}_i \mathbf{z}$ . The objective function can be decomposed as

$$\sum_{k=1}^K \left( \|\mathbf{h}^k\|_{\mathbf{Q}}^2 + \sum_{\substack{i \in \Omega: \\ s(i)=k}} |\hat{u}_i - (\mathbf{h}^k)^T \mathbf{R}_i \mathbf{z}|^2 \right) \quad (7)$$

so that the minimization decouples over  $k$ , where the inner sum is over the subset of pixel locations where filter  $\mathbf{h}^k$  is selected. This means we can solve for each filter independently. Filter selection effectively partitions the training data into  $K$  disjoint subsets, over which each filter is trained. Figure 2 shows an example of what these patch subsets look like.

Training from multiple such observed/target image pairs is similar. We include spatial axial flips and  $90^\circ$  rotations of each observation/target image pair in the training set (effectively multiplying the amount of training data by a factor of 8, for “free”) so that the filters learn symmetries with respect to these manipulations.

The subproblem for each filter  $\mathbf{h}$  takes the following form: let  $\{i(1), \dots, i(M)\}$  enumerate spatial positions where  $s(i) = k$  and  $M$  is the number of such locations, and define  $b_m = x_{i(m)}$  and  $\hat{b}_m = \mathbf{h}^T \mathbf{R}_{i(m)} \mathbf{z}$ . We solve for the filter as

$$\arg \min_{\mathbf{h}} \|\mathbf{h}\|_{\mathbf{Q}}^2 + \|\mathbf{b} - \hat{\mathbf{b}}\|^2. \quad (8)$$

This is simply multivariate linear regression with regularization. We review it briefly here. Defining the design matrix  $A_{m,n} = (\mathbf{R}_m \mathbf{z})_n$  of size  $M \times N$ , the squared residual norm is

$$\begin{aligned} \|\mathbf{b} - \hat{\mathbf{b}}\|^2 &= \sum_{m=1}^M |b_m - \hat{b}_m|^2 \\ &= \sum_{m=1}^M \left| b_m - \sum_{n=1}^N A_{m,n} h_n \right|^2 \\ &= \|\mathbf{b}\|^2 - 2\mathbf{A}^T \mathbf{b} + \|\mathbf{h}\|_{\mathbf{A}^T \mathbf{A}}^2. \end{aligned} \quad (9)$$

The optimal filter is

$$\mathbf{h} = (\mathbf{Q} + \mathbf{A}^T \mathbf{A})^{-1} \mathbf{A}^T \mathbf{b}. \quad (10)$$

---

**Algorithm 1** BLADE training

---

**Input:** Observed image  $\mathbf{z}$  and target image  $\mathbf{u}$

**Output:** Filter  $\mathbf{h}^k$ , residual variance  $\sigma_{\mathbf{r}}^2$ , filter variance estimate  $\Sigma_{\mathbf{h}^k}$

- 1: Determine filter selection  $s$ .
  - 2: Initialize  $\mathbf{G}$  and  $M$  with zeros.
  - 3: **for** each  $i$  where  $s(i) = k$  **do**
  - 4:    $\mathbf{G} \leftarrow \mathbf{G} + \begin{pmatrix} \mathbf{R}_i \mathbf{z} \\ x_i \end{pmatrix} (\mathbf{R}_i \mathbf{z}^T \ x_i)$
  - 5:    $M \leftarrow M + 1$
  - 6: **end for**
  - 7:  $\begin{pmatrix} \mathbf{A}^T \mathbf{A} & \mathbf{A}^T \mathbf{b} \\ \mathbf{b}^T \mathbf{A} & \mathbf{b}^T \mathbf{b} \end{pmatrix} \leftarrow \mathbf{G}$
  - 8:  $\mathbf{h}^k \leftarrow (\mathbf{Q} + \mathbf{A}^T \mathbf{A})^{-1} \mathbf{A}^T \mathbf{b}$
  - 9:  $\sigma_{\mathbf{r}}^2 \leftarrow \frac{1}{M-N} (\mathbf{b}^T \mathbf{b} - 2\mathbf{A}^T \mathbf{b} + \|\mathbf{h}^k\|_{\mathbf{A}^T \mathbf{A}}^2)$
  - 10:  $\Sigma_{\mathbf{h}^k} \leftarrow \sigma_{\mathbf{r}}^2 (\mathbf{Q} + \mathbf{A}^T \mathbf{A})^{-1}$
- 

The variance of the residual  $\mathbf{r} = \mathbf{b} - \hat{\mathbf{b}}$  is estimated as

$$\sigma_{\mathbf{r}}^2 = \frac{1}{M-N} \|\mathbf{b} - \hat{\mathbf{b}}\|^2. \quad (11)$$

Modeling the residual as i.i.d. zero-mean normally distributed noise of variance  $\sigma_{\mathbf{r}}^2$ , an estimate of the filter's covariance matrix is

$$\Sigma_{\mathbf{h}} = \sigma_{\mathbf{r}}^2 (\mathbf{Q} + \mathbf{A}^T \mathbf{A})^{-1}. \quad (12)$$

The square root of the  $j$ th diagonal element estimates the standard deviation of  $h_j$ , which is a useful indication of its reliability. In implementation, it is enough to accumulate a Gram matrix of size  $(N+1)$  by  $(N+1)$ , which allows us to train from any number of examples with a fixed amount of memory. The above algorithm can be used to train multiple filters in parallel.

RAISR [21] is a special case of BLADE where the observations  $\mathbf{z}$  are downsampled versions of the targets  $\mathbf{u}$  and a different set of filters are learned for each subpixel shift.

In the extreme  $K = 1$  of a single filter, the trained filter is the classic Wiener filter [31], the linear minimum mean square estimator relating the observed image to the target. With multiple filters  $K > 1$ , the result is necessarily at least as good in terms of MSE as the Wiener filter. Since filters are trained over different subsets of the data, each filter is specialized for its own distribution of input patches. This distribution may be a much narrower and more accurately modeled than the one-size-fits-all single filter estimator.

BLADE may be seen as a particular two-layer neural network architecture, where filter selection  $s(i)$  is the first layer and filtering with  $\mathbf{h}^{s(i)}$  is the second layer (Figure 1). An essential feature is that BLADE makes a hard decision in which filter to apply. Hard decision is usually avoided intermediately in a neural network since it is necessarily a discontinuous operation, for which gradient-based optimization techniques are not directly applicable.

A conventional network architecture for edge-adaptive filtering would be to use a convolutional neural network (CNN) in which later layers make weighted averages of filtered channels from the previous layer, essentially a soft decision among filters as described for example by Xu et al. [32]. Soft decisions are differentiable and more easily trainable, but requires in a CNN that all filters are evaluated at all spatial positions, so cost increases with the number of filters. On the contrary, BLADE’s inference cost is independent of the number of filters, since for each spatial position only the selected filter is evaluated.

Besides efficient inference, a strength of our approach is interpretability of the trained filters. It is possible to plot the table of filters (examples are shown in Sections 4, 5, 7) and assess the behavior by visual inspection. Defects can be quickly identified, such as inadequate training data or regularization manifest as filters with noisy coefficients, and using an unnecessarily wide support is revealed by all filters having a border of noisy or small coefficients.

### 3 Filter Selection

To make filtering (1) adaptive to image edges and local structure, we perform filter selection  $s$  using features of the  $2 \times 2$  image structure tensor. Ideally, filter selection should partition the input data finely and uniformly enough that each piece of the input data over  $\{i \in \Omega : s(i) = k\}$  is well-approximated by a linear estimator and contains an adequate number of training examples. Additionally, filter selection should be robust to noise and computationally efficient.

We find that structure tensor analysis is an especially good choice: it is robust, reasonably efficient, and works well for a range of tasks that we have tested. The structure tensor analysis is a principle components analysis (PCA) of the local gradients. PCA explains the variation in the gradients along the principal directions. In a small window, one can argue this is all that matters to understand the geometry of the signal. Generically though, any features derived from the input image could be used. For example, the input intensity could be used in filter selection to process light vs. dark regions differently.



### 3.1 Image structure tensor

As introduced by Förstner and Gülch [10] and Bigün and Granlund [2], the image structure tensor (also known as the second-moment matrix, scatter matrix, or interest operator) is

$$J(\nabla u) := \begin{pmatrix} \partial_{x_1} u \\ \partial_{x_2} u \end{pmatrix} \begin{pmatrix} \partial_{x_1} u & \partial_{x_2} u \end{pmatrix}, \quad (13)$$

where in the above formula,  $u(x)$  is a continuous-domain image,  $\partial_{x_1}$  and  $\partial_{x_2}$  are the spatial partial derivatives in each axis, and  $\nabla = (\partial_{x_1}, \partial_{x_2})^T$  denotes gradient. At each point,  $J(\nabla u)(x)$  is a  $2 \times 2$  rank-1 matrix formed as the outer product of the gradient  $\nabla u(x)$  with itself. The structure tensor is smoothed by convolution with Gaussian  $G_\rho$  of standard deviation  $\rho$ ,

$$J_\rho(\nabla u) := G_\rho * J(\nabla u), \quad (14)$$

where the convolution is applied spatially to each component of the tensor. The smoothing parameter  $\rho$  determines the scale of the analysis, a larger  $\rho$  characterizes the image structure over a larger neighborhood.

As described e.g. by Weickert [30], the  $2 \times 2$  matrix at each pixel location of the smoothed structure tensor  $J_\rho(\nabla u)$  is nonnegative definite with orthogonal eigenvectors. This eigensystem is a powerful characterization of the local image geometry. The dominant eigenvector is a robust spatially-smoothed estimate of the gradient orientation (the direction up to a sign ambiguity) while the second eigenvector gives the local edge orientation. The larger eigenvalue is a smoothed estimate of the squared gradient magnitude. In other words, the eigensystem of  $J_\rho(\nabla u)$  is a spatially-weighted principle components analysis of the raw image gradient  $\nabla u$ .

The eigenvalues  $\lambda_1 \geq \lambda_2$  and dominant eigenvector  $\mathbf{w}$  of a matrix  $\begin{pmatrix} a & b \\ b & c \end{pmatrix}$  can be computed as

$$\lambda_{1,2} = \frac{1}{2}((a + c) \pm \delta), \quad (15)$$

$$\mathbf{w} = \begin{pmatrix} 2b \\ c - a + \delta \end{pmatrix}, \quad (16)$$

where<sup>3</sup>  $\delta = \sqrt{(a - c)^2 + (2b)^2}$ . The second eigenvector is the orthogonal complement of  $w$ . From the eigensystem, we define the features:

- orientation =  $\arctan w_2/w_1$ , is the predominant local orientation of the gradient;
- strength =  $\sqrt{\lambda_1}$ , is the local gradient magnitude; and
- coherence =  $\frac{\sqrt{\lambda_1} - \sqrt{\lambda_2}}{\sqrt{\lambda_1} + \sqrt{\lambda_2}}$ , which characterizes the amount of anisotropy in the local structure.<sup>4</sup>

<sup>3</sup>If the matrix is proportional to identity ( $a = c, b = 0$ ), any vector is an eigenvector of the same eigenvalue. In this edge case, (16) computes  $\mathbf{w} = \begin{pmatrix} 0 \\ 0 \end{pmatrix}$ , which might be preferable as an isotropic characterization.

<sup>4</sup>Different works vary in the details of how “coherence” is defined. This is the definition that we use.

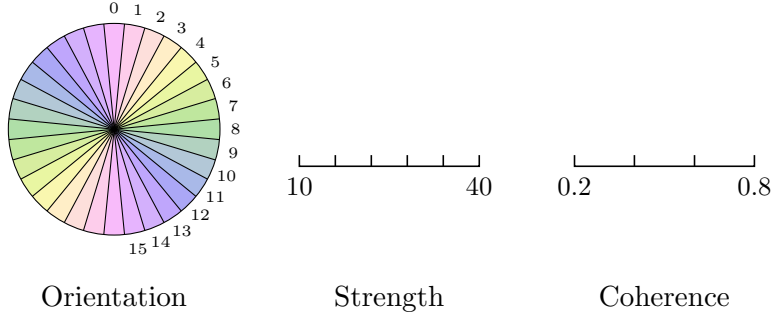


Figure 3: Typical structure tensor feature quantization for BLADE filter selection, using 16 orientations, 5 strength bins, and 3 coherence bins.

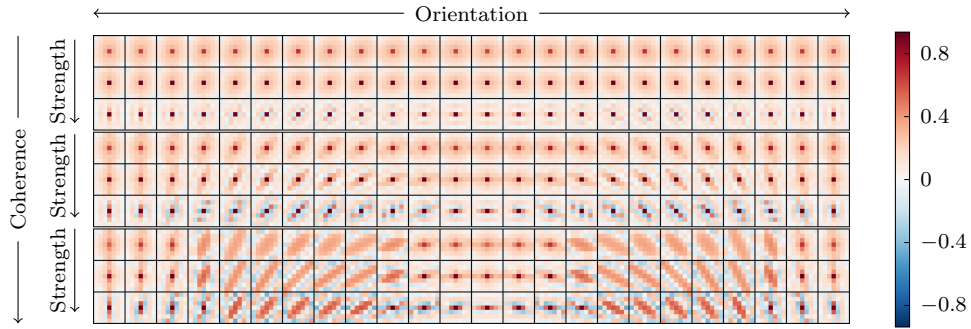


Figure 4: Trained  $7 \times 7$  BLADE filters approximating the bilateral filter with 24 different orientations, 3 strength values, and 3 coherence values.

### 3.2 Quantization

We use the three described structure tensor features for filter selection  $s$ , bounding and uniformly quantizing each feature to a small number of equal-sized bins, and considering them together as a three-dimensional index into the bank of filters.

A typical quantization is shown in Figure 3. The orientation feature is quantized to 16 orientations. To avoid asymmetric behavior, orientation quantization is done such that horizontal and vertical orientations correspond to bin centers. Strength is bounded to  $[10, 40]$  and quantized to 5 bins, and coherence is bounded to  $[0.2, 0.8]$  and quantized to 3 bins.

## 4 Learning for Computational Photography

This and the next few sections show the flexibility of our approach by applying BLADE to several applications. We begin by demonstrating how BLADE can be used to make fast approximations to other image processing methods. BLADE can produce a similar effect that in some cases has lower computational cost than the original method.



Figure 5: Approximation of the bilateral filter. Top row: BLADE has PSNR 35.90 dB and MSSIM 0.9272. Bottom row: BLADE has PSNR 33.41 dB and MSSIM 0.8735.

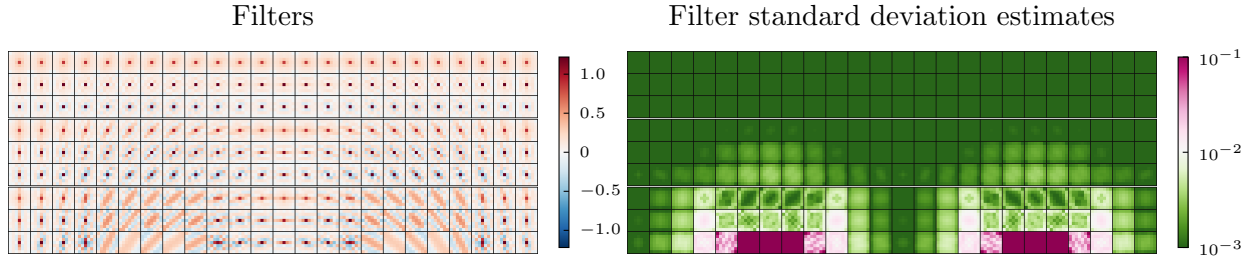


Figure 6: Example of interpreting failed training. Left: filters. Right: filter standard deviation estimates. Compare with Figure 4.

## 4.1 Bilateral filter

The bilateral filter [28] is an edge-adaptive smoothing filter where each output pixel is computed from the input as

$$\hat{u}_i = \frac{\sum_j G_{\sigma_r}(|z_i - z_j|) G_{\sigma_s}(\|i - j\|) z_j}{\sum_j G_{\sigma_r}(|z_i - z_j|) G_{\sigma_s}(\|i - j\|)}, \quad (17)$$

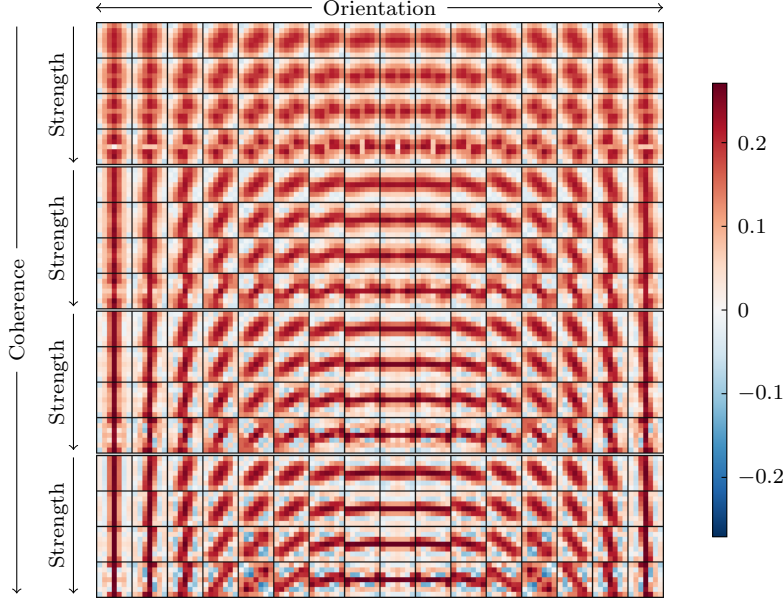


Figure 7:  $7 \times 7$  BLADE filters approximating TV flow with 16 different orientations, 4 strength values, and 4 coherence values.

where  $G_\sigma$  denotes a Gaussian kernel with standard deviation  $\sigma$ .

We approximate the bilateral filter where the range kernel has standard deviation  $\sigma_r = 25$  (relative to a  $[0, 255]$  nominal intensity range) and the spatial kernel has standard deviation  $\sigma_s = 2.5$  pixels. We use  $7 \times 7$  filters, smoothing strength  $\rho = 1.2$ , 24 orientation buckets, 3 strength buckets over  $[10, 35]$ , and 3 coherence buckets over  $[0.2, 0.8]$  (Fig. 4).

Over the Kodak Image Suite, bilateral BLADE agrees with the reference bilateral implementation with an average PSNR of 37.30 dB and average MSSIM of 0.9630 and processing each  $768 \times 512$  image costs 18.6 ms on a Xeon E5-1650v3 desktop PC. For comparison, the domain transform by Gastal and Oliveira [11], specifically developed for efficiently approximating the bilateral filter, agrees with the reference bilateral implementation with an average PSNR of 42.90 dB and average MSSIM of 0.9855 and costs 5.6 ms. Fig. 5 shows BLADE approximation of the bilateral filter on a crop from image 17 and 22 of the Kodak Image Suite.

**Number of filters** With using fewer filters, the BLADE approximation can be made to trade memory cost for accuracy, which may be attractive on resource constrained platforms. For example, training BLADE using instead 8 orientations, 3 strength buckets, and no bucketing over coherence (24 filters vs. 216 filters above), the approximation accuracy is only moderately reduced to an average PSNR of 37.00 dB and MSSIM 0.9609. A reasonable approximation can be made with a small number of filters.





Figure 8: Example of approximated TV flow. Top row: BLADE has PSNR 32.10 dB and MSSIM 0.9369. Bottom row: BLADE has PSNR 35.99 dB and MSSIM 0.9691.

**Interpretability** To demonstrate the interpretability of BLADE, Figure 6 shows a failed training example where we attempted to train BLADE filters for bilateral filtering with strength range over  $[10, 80]$ . Some of the high strength, high coherence buckets received few training patches. Training parameters are otherwise the same as before. The filters are overly-smooth in the problematic buckets. Additionally, the corresponding filter standard deviation estimates are large, indicating a training problem.

## 4.2 TV flow

In this section, we use BLADE to approximate the evolution of an anisotropic diffusion equation, a modification of total variation (TV) flow suggested by Marquina and Osher [16],

$$\partial_t u = |\nabla u| \operatorname{div}(\nabla u / |\nabla u|) \quad (18)$$

where  $u(x)$  is a continuous-domain image,  $\nabla$  denotes spatial gradient,  $\operatorname{div}$  denotes divergence, and  $\partial_t u$  is the rate of change of the evolution.

We train  $7 \times 7$  filters ( $K = 16 \times 4 \times 4$ ) on a dataset of 32 photograph images of size  $1600 \times 1200$ . We use the second-order finite difference scheme described by Marquina and Osher [16] as the reference implementation to generate target images for training (Fig. 7).

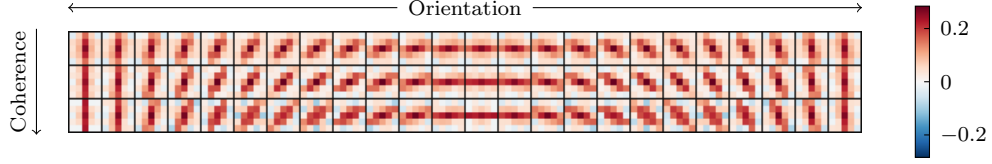


Figure 9:  $5 \times 5$  BLADE filters approximating edge tangent flow with 24 different orientations and 3 coherence values.

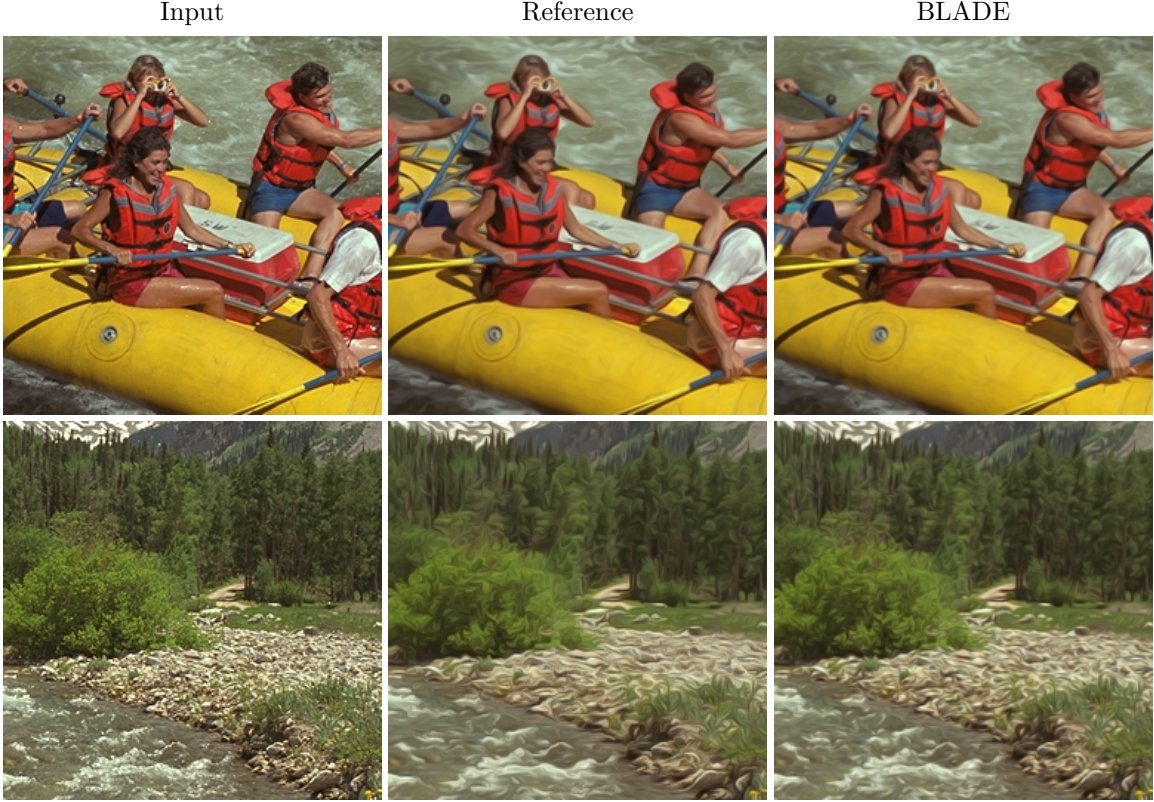


Figure 10: Examples of approximated edge tangent flow. Top row: BLADE has PSNR 39.12 dB and MSSIM 0.9809. Bottom row: BLADE has PSNR 34.80 dB and MSSIM 0.9639.

Over the Kodak Image Suite, the BLADE TV flow approximation agrees with the reference implementation with an average PSNR of 34.77 dB and average MSSIM of 0.9482. Processing each  $768 \times 512$  image costs 17.4 ms on a Xeon E5-1650v3 desktop PC. Fig. 8 shows the filters applied to a crop from image 5 and 8 of the Kodak Image Suite.

### 4.3 Edge tangent flow

Similarly, we can approximate tensor-driven diffusions like edge tangent flow (ETF),

$$\partial_t u = \operatorname{div}(D(u) \nabla u) \quad (19)$$



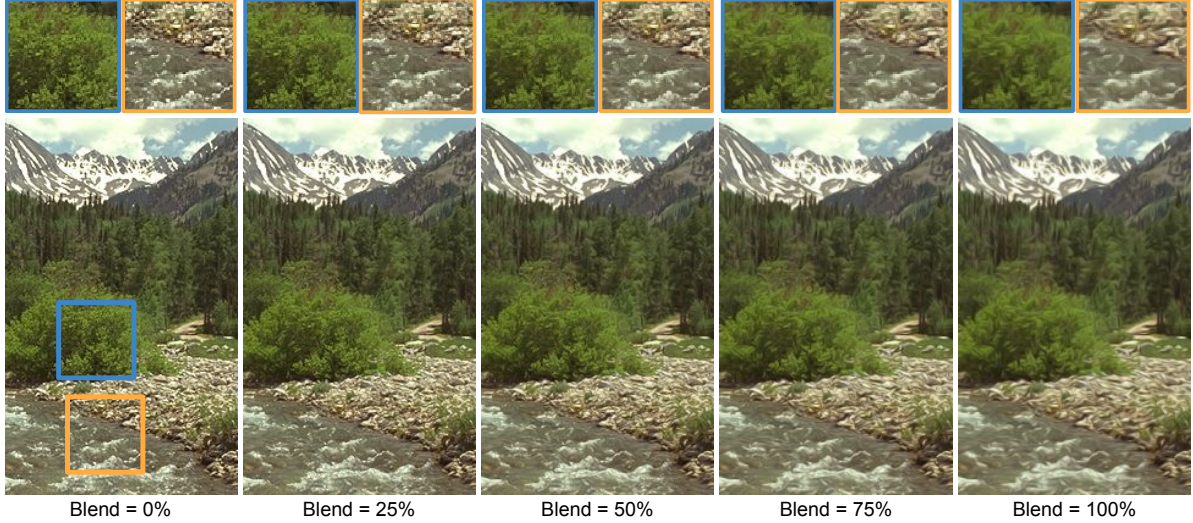


Figure 11: Control filter strength. Blending the identity filter with the edge tangent flow filter.

where at each point,  $D(u)(x)$  is the  $2 \times 2$  outer product of the unit-magnitude local edge tangent orientation. Supposing the edge tangent orientation is everywhere equal to  $\theta$ , the diffusion (19) reduces to the one-dimensional heat equation along  $\theta$ , whose solution is convolution with an oriented Gaussian,

$$u(t, x) = \int_{-\infty}^{\infty} \frac{\exp(-\frac{s^2}{4t})}{\sqrt{4\pi t}} u(0, x + \theta s) ds. \quad (20)$$

We expect for this reason that the structure tensor orientation matters primarily to approximate this diffusion. However, if orientation is not locally constant, the solution is more complicated. Therefore, we use also the coherence, which indicates the extent to which the constant orientation assumption is true (whereas strength gives no such indication, so we exclude it).

We train  $5 \times 5$  filters ( $K = 24 \times 3$ ) over the same dataset, using line integral convolution evolved with second-order Runge–Kutta as a reference implementation to generate target images for training.

Over the Kodak Image Suite, the BLADE ETF approximation agrees with the reference implementation with an average PSNR of 40.94 dB and average MSSIM of 0.9849. Processing each  $768 \times 512$  image costs 14.5 ms on a Xeon E5-1650v3 desktop PC. Figure 10 shows an example application to a crop from image 13 and 14 of the Kodak Image Suite.

#### 4.4 Control the filter strength

One limitation of using these filters for image processing is that each set of filters is trained for a specific set of filter parameters (e.g. our bilateral filter is trained for  $\sigma_r = 25$ ,  $\sigma_s = 2.5$ ),

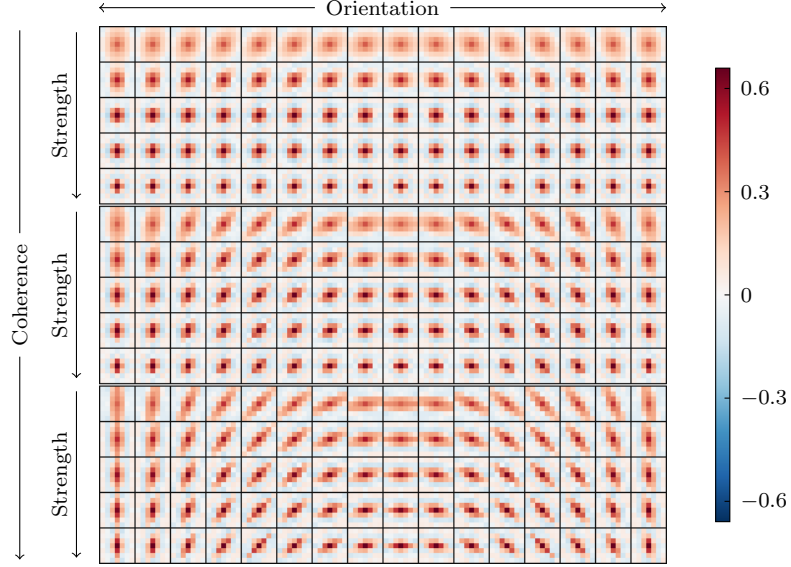


Figure 12:  $7 \times 7$  BLADE filters for AWGN denoising with noise standard deviation 20, using  $\rho = 1.7$ , 16 different orientations, 5 strength values, and 3 coherence values.

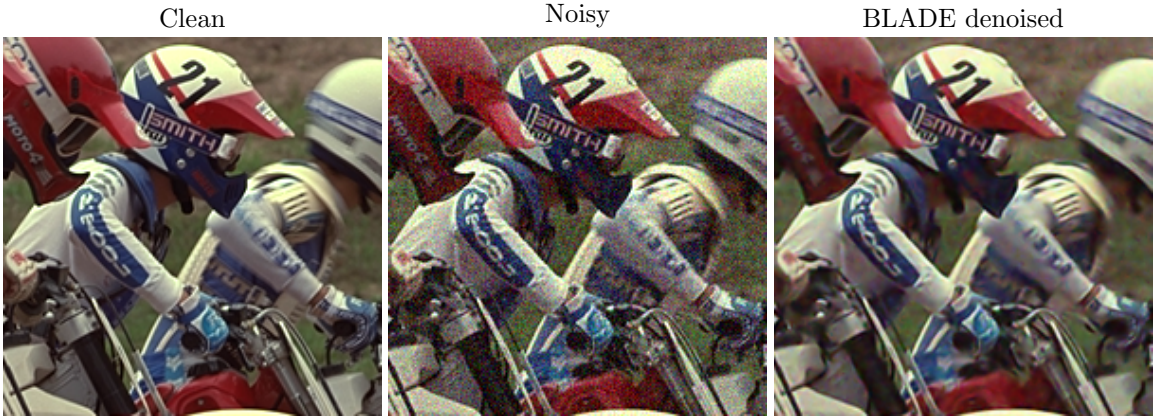


Figure 13: Simple AWGN denoiser example with noise standard deviation 20. The noisy image has PSNR 22.34 dB and MSSIM 0.5792 and the BLADE denoised image has PSNR 28.04 dB and MSSIM 0.8268.

however, it would be interesting to be able to control the strength of the effect without having multiple versions of the filters for different filter parameters. To address this issue, given that each filter knows how to apply the effect for that specific bucket, we interpolate each filter linearly with the identity filter (i.e., a delta in the origin of the filter). Figure 11 shows an example of how we can use this to control the strength of the BLADE ETF filter.

Since we interpolate the filters (which are small compared to the image), the performance penalty is negligible.



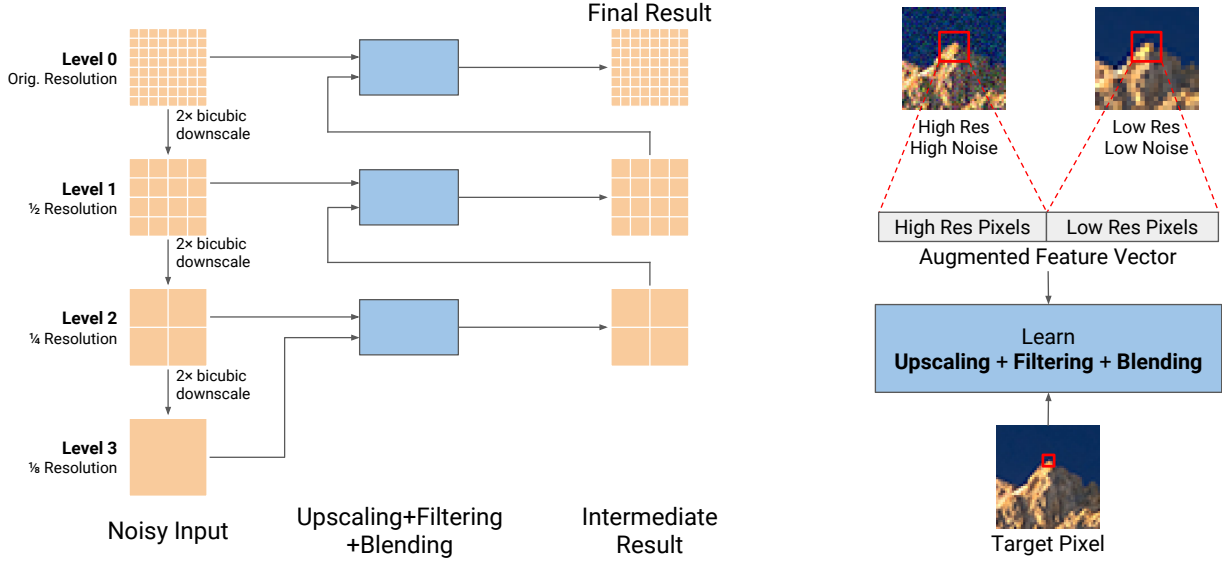


Figure 14: Multilevel BLADE denoising pipeline.

## 5 Denoising

### 5.1 A Simple AWGN Denoiser

We build a grayscale image denoiser with an additive white Gaussian noise (AWGN) model by training a BLADE filter, using a set of clean images as the targets and synthetically adding noise to create the observations.

Filters are selected based on the observed image structure tensor analysis (as described in section 3). Since the observed image is noisy, the structure tensor smoothing by  $G_\rho$  has the critical role of ameliorating noise before computing structure tensor features. Parameter  $\rho$  must be large enough for the noise level to obtain robust filter selection. Figure 12 shows the trained filters for a noise standard deviation of 20, for which we set  $\rho = 1.7$ .

We test the denoiser over the Kodak Image Suite with ten AWGN noise realizations per image. The noisy input images have average PSNR of 22.31 dB and average MSSIM of 0.4030. The simple BLADE denoiser improves the average PSNR to 29.44 dB and MSSIM to 0.7732. Processing each  $768 \times 512$  image costs 19.8 ms on a Xeon E5-1650v3 desktop PC. Figure 13 shows an example of denoising a crop of image 5 from the Kodak Image Suite.

### 5.2 Multiscale AWGN Denoising

We now demonstrate how multiscale application of the previous section enables BLADE to perform fast edge-adaptive image denoising with quality in the ballpark of much more expensive methods. We begin by taking an input image and forming an image pyramid by



Figure 15: Qualitative comparison of denoising results.

downsampling by factor of two. Using a bicubic downsampler, which effectively reduce the noise level by half per level, and is extremely fast. An image pyramid of a target image is also constructed by using the same downsampling method.

Considering level  $L$  as the coarsest level of the image pyramid, we start training from the level  $L - 1$  and go up to the finest level. We train filters that operate on a pair of patches, one from the input image at the current level and another at the corresponding position in the filtered result at the next coarser level, see Figure 14.

We build up denoised results as shown in Figure 14. The filters are learned to optimally upscale coarser level images and blend them into filtered current level images to create results for next level. Structure tensor analysis is performed on the patches of the current level.

Figure 15 shows a comparison of denoising results among other methods. Multiscale denoising results have quality comparable to the state-of-the-art algorithms but with fast processing time.

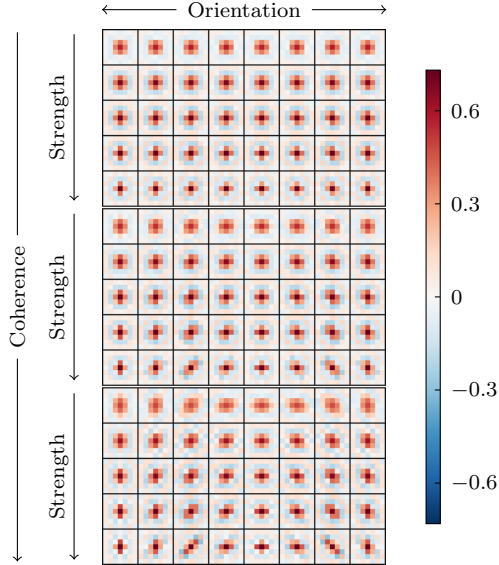


Figure 16:  $7 \times 7$  BLADE filters for JPEG compression artifact removal for JPEG quality level 50, using  $\rho = 1.2$ , 8 different orientations, 5 strength values, and 3 coherence values.



Figure 17: JPEG artifact removal with BLADE for JPEG quality level 50.

## 6 JPEG Artifact Removal

Besides AWGN denoising, BLADE filters can undo other kinds of distortion such as JPEG compression artifacts. We train a BLADE filter, using a set of clean images as the targets and JPEG-compressed versions of the same images with JPEG quality level 50. For simplicity, we train on the luma channel only. At inference time, we use the luma channel for filter selection, then process each RGB color channel independently with those selected filters. A

more complicated scheme could train other sets of filters for the  $C_b$  and  $C_r$  channels.

Fig. 17 shows the filters applied to a crop from image 21 of the Kodak Image Suite. Filtering greatly reduces the visibility of the  $8 \times 8$  block edges and DCT ripples.

JPEG artifact removal is essentially a denoising problem, viewing distortion introduced by the lossy compression as noise. We measure over the Kodak Image Suite that JPEG compression with quality 50 corresponds to an average MSE of 43.6. For comparison, we show the results of the simple AWGN BLADE denoiser from section 5.1 trained for AWGN noise of variance 43.6 (“AWGN BLADE” in Fig. 17). While the AWGN denoiser reduces much of the artifacts, the BLADE trained on JPEG is more effective.

Over the Kodak Image Suite, quality level 50 JPEG compression has average PSNR 32.17 dB. AWGN BLADE improves the average PSNR to 32.66 dB, while JPEG BLADE improves average PSNR to 32.75 dB. Indeed, JPEG noise is not AWGN. This shows BLADE takes advantage of spatial correlations in the noise for which it is trained.

Alternatively, we can account for JPEG’s  $8 \times 8$  block structure by training different filters per pixel coordinate modulo 8. At the memory cost of 64 times more filters compared to the single shift approach above, this extension makes a modest improvement.

## 7 Demosaicing

In this section, we consider the task of demosaicing using BLADE. In the original RAISR formulation, filters are designed only for single-channel images, and operate on the luma channel for color images. Demosaicing requires exploiting correlation between color channels, which we do by computing each output sample as a linear combination of samples from all three channels in the input patch.

For each pixel  $i$ , instead of a single-channel filter  $\mathbf{h}^{s(i)}$  that takes in a single-channel patch and outputs a pixel, we use three filters  $\mathbf{h}^{s(i),r}$ ,  $\mathbf{h}^{s(i),g}$ , and  $\mathbf{h}^{s(i),b}$  that compute output red, green, and blue pixels respectively from a given RGB input patch. The resulting inference becomes:

$$\begin{aligned}\hat{u}_i^r &= (\mathbf{h}^{s(i),r})^T \mathbf{R}_i \mathbf{z} \\ \hat{u}_i^g &= (\mathbf{h}^{s(i),g})^T \mathbf{R}_i \mathbf{z} \\ \hat{u}_i^b &= (\mathbf{h}^{s(i),b})^T \mathbf{R}_i \mathbf{z}\end{aligned}\tag{21}$$

where  $\mathbf{R}_i$  extracts a color patch centered at  $i$ , and  $\hat{u}_i^r$ ,  $\hat{u}_i^g$ , and  $\hat{u}_i^b$  denote the output red, green, and blue pixels. We interpret this extension as three separate BLADE filterbanks described in Section 2, one for each output color channel.

With this color extension, we then train filters to exploit correlations between color channels for demosaicing. Similar to RAISR upscaling, we first apply a fast cheap demosaicing on the input image, then perform structure tensor analysis and filter selection as usual. For our experiments we use the method described in Menon et al. [17].

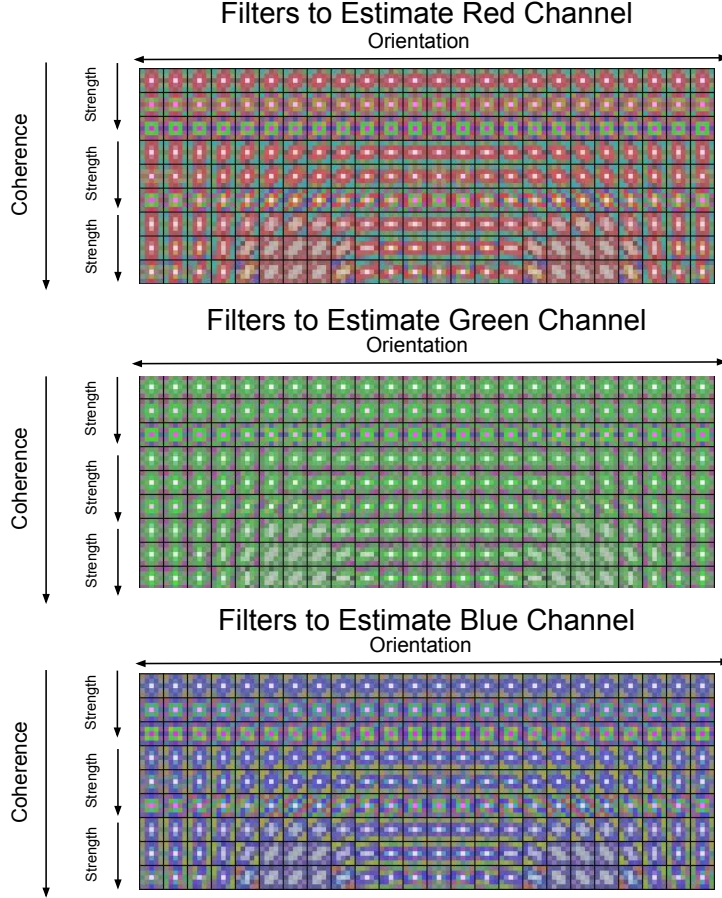


Figure 18: Color BLADE filters trained on Menon demosaiced images, with  $\rho = 0.7$ , 8 difference orientations, 3 strength values, and 3 coherence values. Here, the color map uses the red, green, and blue components of the filters.

Figure 18 shows the color filters trained on Bayer demosaiced images using the method from Menon et al. [17] on the Kodak Image Suite, with  $\rho = 0.7$ , 8 different orientations, 3 strength values, and 3 coherence values. Three sets of color filters were trained to predict red, green, and blue pixels respectively. As expected, the filters to estimate each color channel mostly utilize information from the same color channel. For example, the color filters to estimate red channel are mostly red. On the other hand, cross-channel correlation is leveraged as the filters are not purely red, green, or blue.

We evaluate the demosaicing methods on the Kodak Image Suite. The average PSNR for Menon demosaiced images is 39.14 dB, whereas the average PSNR for our proposed method is 39.69 dB. Figure 19 shows a cropped example with reduction of demosaicing artifacts using our proposed method.



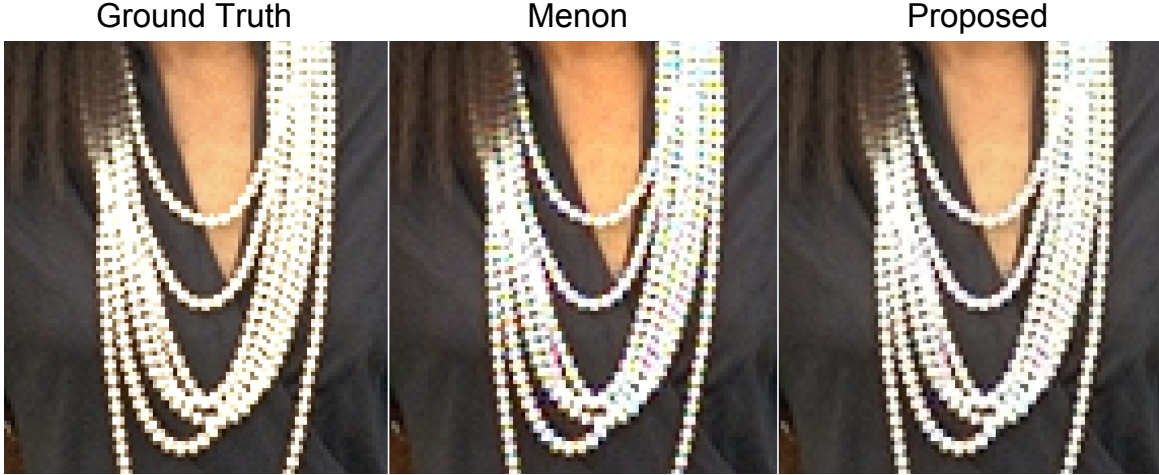


Figure 19: Comparison between Menon and BLADE. Demosaicing with BLADE displays less artifacts.

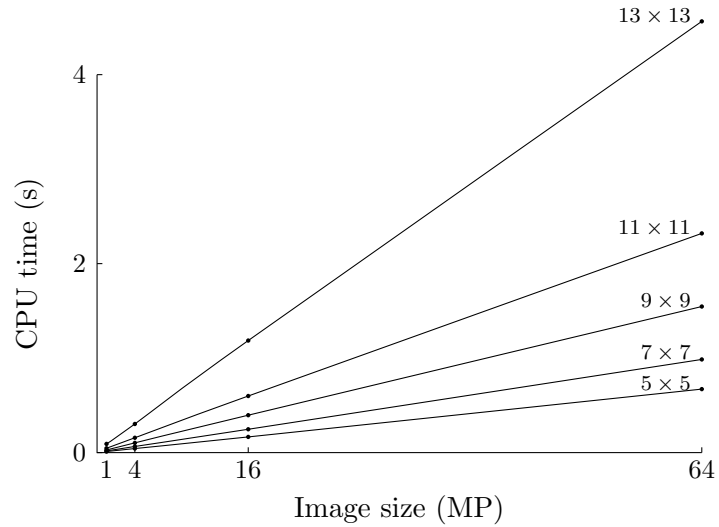


Figure 20: CPU time on Xeon E5-1650v3 desktop PC vs. image size in megapixels.

## 8 Computational Performance

BLADE filtering has been optimized to run fast on desktop and mobile platforms. The optimizations to achieve the desired performance are the following:

- For CPU implementation, the code is optimized using the programming language Halide [19]. Halide code decouples the algorithm implementation from the scheduling. This allows us to create optimized code that uses native vector instructions and parallelizes over multiple CPU cores.

Table 1: CPU performance on different devices.

Platform	$5 \times 5$ filters	$7 \times 7$ filters	$9 \times 9$ filters	$11 \times$ filters	$13 \times 13$ filters
Xeon E5-1650v3 PC	97.50 MP/s	71.70 MP/s	52.26 MP/s	41.28 MP/s	31.00 MP/s
Pixel 2017	29.47 MP/s	22.41 MP/s	18.00 MP/s	15.01 MP/s	11.39 MP/s
Pixel 2016	21.39 MP/s	15.62 MP/s	11.42 MP/s	8.71 MP/s	6.59 MP/s
Nexus 6P	19.06 MP/s	14.60 MP/s	11.09 MP/s	9.11 MP/s	6.72 MP/s

- BLADE processing on the CPU is performed using low-precision integer arithmetic where possible. This allows for a higher degree of vectorization, especially on mobile processors, and reduces memory bandwidth. Analogously, the GPU implementation uses 16-bit float arithmetic where possible.
- The algorithm is GPU amenable, we have seen up to an order of magnitude performance improvement on GPU over our CPU implementation. The BLADE filter selection maps efficiently to texture fetches with all filter coefficients stored in a single RGBA texture. It is also possible to process 4 pixels in parallel per pixel shader invocation by taking advantage of all 4 RGBA channels for processing.
- Approximations to transcendental functions are used where applicable. For example the arctangent for orientation angle computation uses a variation of a well-known quadratic approximation [20].

Our algorithm has runtime linear in the number of output pixels. Figure 20 shows that given a fixed filter size, the performance is linear.

Table 1 shows the performance of BLADE for different platforms on the CPU and different filter sizes. A full HD image ( $1920 \times 1080$  pixels) takes less than 60 ms to process on the mobile devices we tested.

The GPU implementation focuses on the  $5 \times 5$  filters, the peak performance are as follows: 131.53 MP/s on a Nexus 6P, 150.09 MP/s on a Pixel 2016, 223.03 MP/s on a Pixel 2017. Another way to look at it is that the algorithm is capable of 4k video output ( $3840 \times 2160$  pixels) at 27 fps or at full HD output at over 100 fps on device.

## 9 Conclusions

We have presented Best Linear Adaptive Enhancement (BLADE), a framework for simple, trainable, edge-adaptive filtering based on a local linear estimator. BLADE has computationally efficient inference, is easy to train and interpret, and is applicable to a fairly wide range of tasks. Filter selection is not trained; it is performed by hand-crafted features derived from the image structure tensor, which are effective for adapting behavior to the local image geometry, but is probably the biggest weakness of our approach from a machine learning perspective and an interesting aspect for future work.

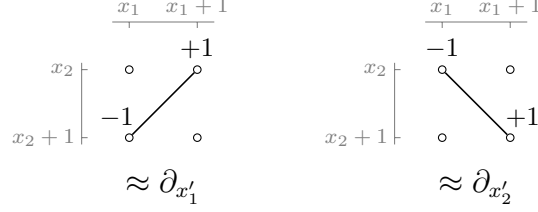


Figure 21: Diagonal finite differences for approximating the image gradient.

## A Numerical details

Implementation of (13) requires a numerical approximation of the image gradient. Forward (or backward) differences could be used, but they are only first-order accurate,

$$\frac{1}{h}(u(x_1 + 1, x_2) - u(x_1, x_2)) = \partial_{x_1} u(x_1, x_2) + \frac{1}{2} \partial_{x_1}^2 u(x_1, x_2) h + O(h^2), \quad (22)$$

where  $h$  is the width of a pixel. Centered differences are second-order accurate, but they increase the footprint of the approximation

$$\frac{1}{2h}(u(x_1 + 1, x_2) - u(x_1 - 1, x_2)) = \partial_{x_1} u(x_1, x_2) + \frac{1}{12} \partial_{x_1}^3 u(x_1, x_2) h^2 + O(h^4) \quad (23)$$

We instead approximate derivatives of 45°-rotated axes  $x' = \frac{1}{\sqrt{2}} \begin{pmatrix} 1 & -1 \\ 1 & 1 \end{pmatrix} x$  with diagonal differences as depicted in Figure 21. If interpreted as logically located at cell centers, diagonal differences are second-order accurate,

$$\frac{1}{\sqrt{2}h}(u(x_1 + 1, x_2) - u(x_1, x_2 + 1)) = \partial_{x'_1} u(x_1 + \frac{1}{2}, x_2 + \frac{1}{2}) + O(h^2), \quad (24)$$

$$\frac{1}{\sqrt{2}h}(u(x_1 + 1, x_2 + 1) - u(x_1, x_2)) = \partial_{x'_2} u(x_1 + \frac{1}{2}, x_2 + \frac{1}{2}) + O(h^2). \quad (25)$$

We then carry out structure tensor analysis on this 45°-rotated and 1/2-sample shifted gradient approximation. When smoothing with  $G_\rho$ , a symmetric even-length FIR filter is used in each dimension to compensate for the +1/2 shift. The eigenvector  $\mathbf{w}$  is rotated back by 45° to compensate for the rotation,  $\tilde{\mathbf{w}} = \begin{pmatrix} 1 & 1 \\ -1 & 1 \end{pmatrix} \mathbf{w}$ .

## References

- [1] Yoshua Bengio. Learning deep architectures for AI. *Foundations and Trends in Machine Learning*, 2(1):1–127, 2009.
- [2] Josef Bigun and Gosta H. Granlund. Optimal orientation detection of linear symmetry. In *IEEE First International Conference on Computer Vision*, pages 433–438, London, Great Britain, 1987.
- [3] Antoni Buades, Bartomeu Coll, and J-M Morel. A non-local algorithm for image denoising. In *IEEE Computer Society Conference on Computer Vision and Pattern Recognition, 2005*, volume 2, pages 60–65. IEEE, 2005.



- [4] Priyam Chatterjee and Peyman Milanfar. Clustering-based denoising with locally learned dictionaries. *IEEE Transactions on Image Processing*, 18(7):1438–1451, 2009.
- [5] Yunjin Chen and Thomas Pock. Trainable nonlinear reaction diffusion: A flexible framework for fast and effective image restoration. *IEEE Transactions on Pattern Analysis and Machine Intelligence*, 39(6):1256–1272, 2017.
- [6] Jae-Seok Choi and Munchurl Kim. Single image super-resolution using global regression based on multiple local linear mappings. *IEEE Transactions on Image Processing*, 26(3):1300–1314, 2017.
- [7] K. Dabov, A. Foi, V. Katkovnik, and K. Egiazarian. Image denoising by sparse 3-D transform-domain collaborative filtering. *IEEE Transactions on Image Processing*, 16(8):2080–2095, 2007.
- [8] Kostadin Dabov, Alessandro Foi, Vladimir Katkovnik, and Karen O Egiazarian. Image restoration by sparse 3D transform-domain collaborative filtering. In *Image Processing: Algorithms and Systems*, page 681207, 2008.
- [9] Joan Duran and Antoni Buades. Self-similarity and spectral correlation adaptive algorithm for color demosaicking. *IEEE transactions on image processing*, 23(9):4031–4040, 2014.
- [10] Wolfgang Förstner and Eberhard Gülch. A fast operator for detection and precise location of distinct points, corners and centres of circular features. In *Proceedings of the Intercomission Conference on Fast Processing of Photogrammetric Data*, pages 281–305, 1987.
- [11] Eduardo SL Gastal and Manuel M Oliveira. Domain transform for edge-aware image and video processing. In *ACM Transactions on Graphics (ToG)*, volume 30, page 69. ACM, 2011.
- [12] Saul B. Gelfand and C.S. Ravishanker. A tree-structured piecewise linear adaptive filter. *IEEE Transactions on Information Theory*, 39(6):1907–1922, 1993.
- [13] Haomiao Jiang, Qiyuan Tian, Joyce Farrell, and Brian Wandell. Learning the image processing pipeline. *IEEE Transactions on Image Processing*, 2017.
- [14] Yifei Lou, Xiaoqun Zhang, Stanley Osher, and Andrea Bertozzi. Image recovery via nonlocal operators. *Journal of Scientific Computing*, 42(2):185–197, 2010.
- [15] Stéphane Mallat. Understanding deep convolutional networks. *Philosophical Transactions of the Royal Society A*, 374(2065):20150203, 2016.
- [16] Antonio Marquina and Stanley Osher. Explicit algorithms for a new time dependent model based on level set motion for nonlinear deblurring and noise removal. *SIAM Journal on Scientific Computing*, 22(2):387–405, 2000.

- [17] Daniele Menon, Stefano Andriani, and Giancarlo Calvagno. Demosaicing with directional filtering and a posteriori decision. *IEEE Transactions on Image Processing*, 16(1):132–141, 2007.
- [18] Grégoire Montavon, Mikio L. Braun, and Klaus-Robert Müller. Kernel analysis of deep networks. *Journal of Machine Learning Research*, 12(Sep):2563–2581, 2011.
- [19] Jonathan Ragan-Kelley, Andrew Adams, Sylvain Paris, Marc Levoy, Saman Amarasinghe, and Frédo Durand. Decoupling algorithms from schedules for easy optimization of image processing pipelines. *ACM Trans. Graph.*, 31(4):32:1–32:12, July 2012.
- [20] S. Rajan, S. Wang, R. Inkol, and A. Joyal. Efficient approximations for the arctangent function. *IEEE Signal Processing Magazine*, pages 108–111, May 2006.
- [21] Yaniv Romano, John Isidoro, and Peyman Milanfar. RAISR: Rapid and Accurate Image Super Resolution. *IEEE Transactions on Computational Imaging*, 3(1):110–125, 2017.
- [22] Stefan Roth and Michael J Black. Fields of experts. *International Journal of Computer Vision*, 82(2):205–229, 2009.
- [23] Sean Ryan Fanello, Cem Keskin, Pushmeet Kohli, Shahram Izadi, Jamie Shotton, Antonio Criminisi, Ugo Pattacini, and Tim Paek. Filter forests for learning data-dependent convolutional kernels. In *Proceedings of the IEEE Conference on Computer Vision and Pattern Recognition*, pages 1709–1716, 2014.
- [24] Hanno Scharr, Michael J. Black, and Horst W. Haussecker. Image statistics and anisotropic diffusion. In *International Conference on Computer Vision 2003*, 2003.
- [25] Uwe Schmidt and Stefan Roth. Shrinkage fields for effective image restoration. In *Proceedings of the IEEE Conference on Computer Vision and Pattern Recognition*, pages 2774–2781, 2014.
- [26] Samuel Schuler, Christian Leistner, and Horst Bischof. Fast and accurate image upscaling with super-resolution forests. In *Proceedings of the IEEE Conference on Computer Vision and Pattern Recognition*, pages 3791–3799, 2015.
- [27] Ioannis M. Stephanakis, George Stamou, and Stefanos Kollias. Piecewise Wiener filter model based on fuzzy partition of local wavelet features for image restoration. In *International Joint Conference on Neural Networks 1999*, volume 4, pages 2690–2693. IEEE, 1999.
- [28] Carlo Tomasi and Roberto Manduchi. Bilateral filtering for gray and color images. In *Sixth International Conference on Computer Vision, 1998*, pages 839–846. IEEE, 1998.
- [29] Shengjie Wang, Abdel-rahman Mohamed, Rich Caruana, Jeff Bilmes, Matthai Philipose, Matthew Richardson, Krzysztof Geras, Gregor Urban, and Ozlem Aslan. Analysis of deep neural networks with extended data Jacobian matrix. In *International Conference on Machine Learning*, pages 718–726, 2016.

- [30] Joachim Weickert. *Anisotropic diffusion in image processing*, volume 1. Teubner Stuttgart, 1998.
- [31] Norbert Wiener. *Extrapolation, interpolation, and smoothing of stationary time series*, volume 7. MIT Press, Cambridge, MA, 1949.
- [32] Li Xu, Jimmy Ren, Qiong Yan, Renjie Liao, and Jiaya Jia. Deep edge-aware filters. In *Proceedings of the 32nd International Conference on Machine Learning (ICML-15)*, pages 1669–1678, 2015.
- [33] Guoshen Yu, Guillermo Sapiro, and Stéphane Mallat. Solving inverse problems with piecewise linear estimators: From Gaussian mixture models to structured sparsity. *IEEE Transactions on Image Processing*, 21(5):2481–2499, 2012.
- [34] Song Chun Zhu and David Mumford. Prior learning and Gibbs reaction-diffusion. *IEEE Transactions on Pattern Analysis and Machine Intelligence*, 19(11):1236–1250, 1997.